PHYSICAL REVIEW B **70**, 144514 (2004)

Critical state in superconducting single-crystalline $YBa_2Cu_3O_7$ foams: Local versus long-range currents

E. Bartolomé, X. Granados, T. Puig, and X. Obradors
Institut de Ciència de Materials de Barcelona, C.S.I.C. Campus U.A.Barcelona, 08193 Bellaterra, Spain

E. S. Reddy and G. J. Schmitz
ACCESS e.V. Materials & Processes, Intzestrasse 5, D-52072 Aachen, Germany

(Received 28 July 2003; revised manuscript received 16 April 2004; published 22 October 2004)

The establishment of the critical state in single-crystalline $YBa_2Cu_3O_7$ foams, a new kind of porous superconducting material, has been analyzed by using Hall probe magnetic imaging and hysteresis cycles. We evidence that superconducting foams display a critical state composed of a background magnetization linked to the total dimension of the sample, superposed to many additional magnetic flux peaks related to the pore structure of the foam. The observed magnetization maps can be described by an "effective," long-range critical-current density extending over the whole sample and a local critical-current density associated with small current loops. The values of the effective critical current density are mainly determined by the amount of porosity. The magnetic field dependence of the local and effective critical-current densities are found to be the same and independent on sample porosity, indicating that vortex pinning is the only physical microscopic mechanism ruling the critical currents in these materials.

DOI: 10.1103/PhysRevB.70.144514 PACS number(s): 74.81.Bd, 74.25.Sv

I. INTRODUCTION

Since the early 1960s, the critical state model[1] has been a unique tool to analyze the irreversible behavior of the mixed state of type II superconductors. The model assumes that, due to the existence of vortex pinning centers, a magnetic flux gradient is generated in the superconductor and hence Ampère's law imposes the existence of bulk currents: $\nabla \times \mathbf{B} = (4\pi/c)\mathbf{J}$. In the simplest approximation, these currents are assumed to be field independent and a constant critical-current density J_c circulates in those regions where magnetic flux has penetrated. The application of this model to many simple geometrical shapes of superconductors[2–4] has greatly advanced our knowledge of the macroscopic behavior of high-temperature superconductors; however, the applicability to complex geometries is not straightforward. The recent discovery of a new form of superconducting material, the single-crystalline superconducting foams,[5,6] represents a very exciting challenge both from a basic and applied point of view. A superconducting foam can be described as a single crystal with a multiple connected geometry, i.e., an open porous structure where thin struts percolate all along the sample. A potential advantage of these structures for practical applications relies on their high specific surface area, which will enhance the thermal stability, hence ameliorating the performances for fault current limitation.[7,8]

From a fundamental point of view, superconducting foams additionally raise many interesting questions associated with the effect of the disordered geometry on the morphology of the vortex line lattice and the influence of their high surface-volume ratio on vortex motion. The first new theoretical challenge raised is the study of the applicability of the critical state model. The primary technique to analyze the current-carrying properties is to visualize the magnetic flux gradients and then evaluate the critical current density by applying Ampère's law. In this work we report an investigation of the irreversible magnetic behavior of single-crystalline $YBa_2Cu_3O_7$ superconducting foams by means of an in-field Hall probe magnetic imaging system. We will show that a critical state is established, such that can be described by the circulation of an "effective" long-range current accounting for the full field penetration till the center of the sample, and local short-range currents giving rise to local magnetization peaks. The observed behavior is, though, fundamentally different from the double critical state describing granular polycrystalline superconducting ceramics,[9] since only a single local critical-current density exists in a foam which will be associated with vortex pinning, while those of polycrystalline ceramics arise from intragranular Abrikosov vortex pinning and intergranular Josephson junction currents through a grain boundary network.

II. EXPERIMENTAL DETAILS

The superconducting foams were prepared following a two-step process.[5] In the first step, a porous Y_2BaCuO_5 "skeleton" foam is made by an established ceramic foam fabrication process as follows. A polyurethane foam with the desired porosity is impregnated in a Y_2BaCuO_5 slurry, formed by mixing commercially available Y_2BaCuO_5 powder (1–5 μm size) in a water-based solution with 5 wt. % polyvinyl-alcohol as binder. A thermal process follows such that (i) the organic components (polyvinylalcohol and polyurethane) are burnt off by slow heating at 50 K/h to 600 °C and dwelling during 6 h, and (ii) the resulting Y_2BaCuO_5 ceramic is densified by further heating at 150 K/h to 1.373 K. In the second step, the formed Y_2BaCuO_5 foam is converted into a single-domain

TABLE I. Superconducting $YBa_2Cu_3O_7$ foams studied. Sample dimensions $a\times b\times c$, pore diameter $2R_h$, pore density δ, and relative cross-section density A_S/A_T.

Sample	Dimensions $a\times b\times c$ (mm)	$2R_h$ (mm)	δ (pores/mm^2)	A_S/A_T
Foam A	$23.8\times19.1\times8.3$	2.6	0.15	0.23
Foam B	$17.0\times12.0\times7.5$	1.6	0.28	0.43
Foam C	$2.8\times2.8\times2.8$	0.65	1.48	0.51

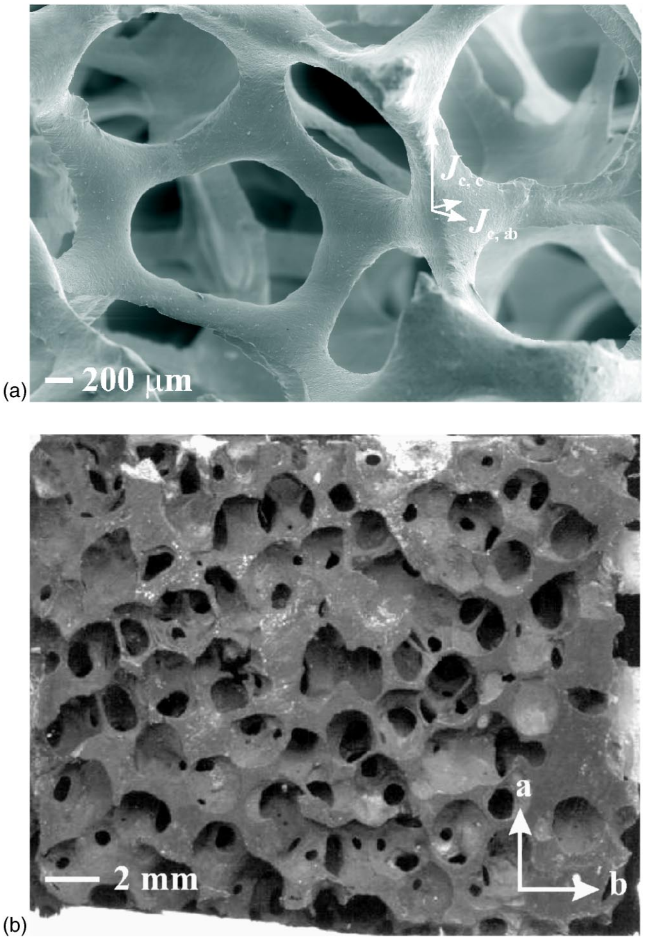

FIG. 1. (a) SEM micrograph showing the typical three-dimensional structure of a foam, where the pores and the struts are observed. (b) Optical microscopy image of a polished surface of an *ab* plane of foam A.

$YBa_2Cu_3O_7$ foam by an infiltration process[10,5] followed by a top-seeding growth (TSG) method,[11–13] commonly used for the growth of melt-textured single domains. In this process a liquid phase source, formed by a mixture (1:1) of barium and copper oxides and additional $YBa_2Cu_3O_7$ powder, is placed under the Y_2BaCuO_5 foam, and the assembly is heated up above the peritectic temperature (1010 °C). The $YBa_2Cu_3O_7$ phase decomposes into solid Y_2BaCuO_5 and liquid phase, which infiltrates into the Y_2BaCuO_5 skeleton by capillarity.[14] The infiltrated Y_2BaCuO_5 foam is then slowly cooled down (0.3 K/h) through the peritectic temperature with a $NdBa_2Cu_3O_{7-x}$ seed crystal centered on top of it, resulting in the growth of a single-crystalline $YBa_2Cu_3O_7$ foam. The single-crystalline structure of the foam is evidenced by the intense (001) peaks observed in the $\theta-2\theta$ x-ray diffraction pattern and by the fourfold symmetric (103) pole figure.[5] The final foam porosity can be tuned by selecting the initial polystyrene foam. Three samples have been studied, with different pore radius R_h and pore surface density δ (Table I). These two parameters were estimated by measuring, respectively, the average radius and number of holes in several foam cross-section images obtained by optical microscopy. The relative surface density, or fraction of superconducting area A_S in a cross section of total area A_T, is then: $A_S/A_T=1-(\pi R_h^2)\delta$. Figures 1(a) and 1(b) show typical SEM and optical microscopy images of superconducting foams.

The magnetic characterization of foams was done with a Hall probe scanning system able to measure the local magnetic induction $B_z(x,y)$ under magnetic fields up to 1 T applied parallel to the c axis of the single-crystalline foam.[15] An AsGa Hall probe with an active area of $0.1\times0.1\ \mathrm{mm}^2$ sweeps the sample surface at a flying distance of $\sim80\ \mu$m in steps of 160 μm. The local "magnetization" is obtained by subtracting the applied field at every point: $B_z(x,y)-H$. The integration of $B_z(x,y)-H$ over the scanned sample area S should be proportional to the total sample magnetization M

$$\overline{B}-H=\frac{1}{S}\int\int[B_z(x,y)-H]dx\,dy=k^{-1}M, \tag{1}$$

through the proportionality constant k^{-1}, which depends on the geometry of the sample and the height of the scanning Hall probe. We have shown in a recent work that a single constant k^{-1} is needed to correlate the Hall integrated magnetization $[\overline{B}-H](H)$ to the $M(H)$ measured with a SQUID magnetometer.[15] The factor k of the foams in this work was determined theoretically as follows. A numerical method[16] was applied to obtain the distribution of currents in the sample, assumed cylindrical and pore-free. The demagnetization effects are hence taken into account. The model divides the sample in cylindrical paths of constant current, and uses energy minimization to solve the current distribution, from which the integrated $[\overline{B}-H](0)$ at the Hall probe flying distance is calculated. On the other hand, $M(0)$ is obtained from the standard Bean equation for a cylinder ($J_c\approx30\,M/R$); k is then just the ratio: $k=M(0)/[\overline{B}-H](0)$.

The Hall probe scanning set up allows both measuring the remanent magnetization after a field-cool process (fc) under a maximum applied field, or measuring the integrated magnetization after a zero-field-cool process at different applied fields along a hysteresis cycle. In some cases the magnetic moment of foams was also measured with a commercial ("Quantum Design PPMS") magnetometer.

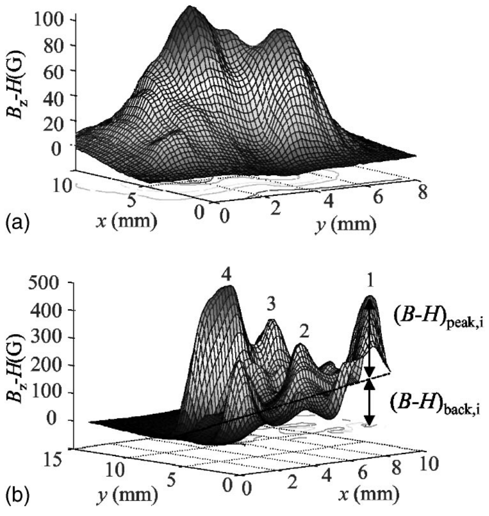

FIG. 2. Local magnetization distributions in the remanent state determined with a Hall probe magnetic imaging system: (a) 3D magnetic flux profile of foam B; (b) 3D magnetic flux profile of foam A (only $\frac{1}{4}$ of the total scan is shown). Several peaks used for the determination of the $[(B\text{-}H)_{\text{peak}}/R_{\text{peak}}]_{\text{i}}$ slopes of the local magnetization peaks (marked 1 to 4) and the slope $(B\text{-}H)_{\text{back}}/\ R)$ of the background magnetization are indicated. The typical radius of the small-size loops is ~1.5 mm.

III. RESULTS AND DISCUSSION

A. Local and effective currents in the remanent state

The foams were cooled to 77 K under an $H=0.6$ kOe field, applied perpendicular to the *ab* plane. The remanent magnetization Hall profiles measured showed typically the superposition of a broad peak and several sharp magnetization peaks [Fig. 2(a)]. Analyzing the optical microscopy images of several foam *ab* cross sections, we observed that there were hardly any in-plane percolative connected paths. By further studying the superposition of the remanent magnetic Hall images with optical images of the sample surfaces, we realized that there was not always a good correspondence between the position of the local peaks and the "islands" of superconducting material between the pores. We interpret these results as follows. When a magnetic field H_z (higher than the critical magnetic field H_{c1}) is applied to the foam, a three-dimensional (3D) supercurrent percolates through the sample and a large 3D loop closing the outermost limits of the sample appears. The geometrical inhomogeneity of the foam sample and the condition of current continuity enforce that the current has some *z* component. In contrast, only *ab* planar currents would circulate in a homogeneous, infinitely long sample containing columnar holes. The currents percolate with current density J_c^{ab} in the planar regions and current density J_c^{c} through the vertical struts (Fig. 3). As H_z increases and the sample becomes more and more penetrated, several short-range current paths enclosing small areas are left aside. If an external magnetic field is applied to the sample and then switched off, a critical state flux profile is established that produces a remanent field **B**. The Hall probe imaging system measures only the B_z component. Hence, the current paths flowing along the *z* axis which generate magnetic fields without *z* component will not be sensed by the Hall probe system. Though the real circulating current is 3D, only its *ab* "projection" will be recorded. The contribution of the different current loops to the magnetization Hall probe image is weighted by the area enclosed by the loops and the vertical distance to the sample surface. The sum of all the inductive contributions gives, as a result, a magnetic flux profile [Fig. 2(b)] that can be interpreted in the remanent state as the combination of a background critical state pyramid extended over the basis of the whole sample and several highly localized sharper peaks. This suggests that we can define first an effective critical-current density J_c^{eff} extended over the whole sample and producing the background magnetization observed (Fig. 3). The sharp magnetization peaks then would be produced by the projection of the short-range current loops, with a critical-current density J_c^{ab} characteristic of the material. The effective critical-current density J_c^{eff} would describe the long-range current loops extending over the sample, and hence would be related to the geometry of the sample and the porous structure. We emphasize that though it is convenient to describe the critical state of the foams in terms of two different critical current densities, locally a unique physical critical-current density exists in the single-crystalline foam.

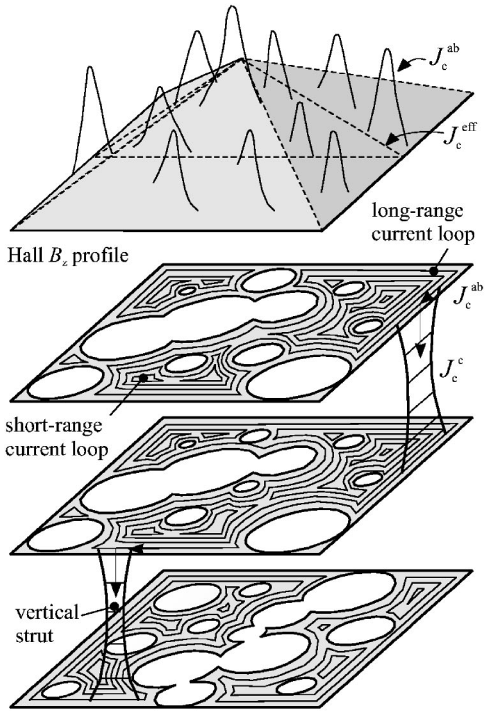

FIG. 3. Schematics of the 3D critical state established in a foam in the remanence. Bottom: Long-range current loop running extending over the sample, with true critical current J_c^{ab} in the *ab* planes and J_c^{c} at the vertical struts. Short-range current loops (also 3D but more limited in space) formed as flux penetrates the sample. Top: Sketch of the magnetic flux B_z profile that would be measured by Hall probe scanning. Local magnetization peaks (with slope $\propto J_c^{ab}$) and background magnetization pyramid, that can be interpreted as generated by the effective critical current density J_c^{eff}.

We used first the critical-state model to evaluate the local and effective critical-current densities. Cgs units are used all through the article. In the Bean approximation to the critical state, and assuming the sample to be a cylinder of radius R, the critical-current density J_c can be estimated as[17,18] $J_c \approx 30\Delta M/2R$, where $\Delta M = M^+ - M^-$ is the width of the magnetization hysteresis loop at a certain field H. The effective J_c^{eff} is determined by definition from the slope (M_{back}/R) of the background magnetization profile in the remanent state

$$J_c^{eff} \approx 30 \cdot \frac{M_{back}}{R} = 30 \cdot \frac{(B-H)_{back}}{R} \cdot k. \qquad (2)$$

For foam A we estimated, for instance, a factor $k \approx 0.256$, and an effective current density of $J_c^{\mathrm{eff}}(0) \approx 1.5 \times 10^3$ A/cm^2.

In a similar way, the local critical-current density J_c^{ab} was estimated from the slope of the magnetization $(M_{\mathrm{peak}}/R_{\mathrm{peak}})_{\mathrm{i}}$ at each one of the sharp peaks measured

$$J_c^{ab,i} \approx 30 \cdot \left(\frac{M_{peak}}{R_{peak}}\right)_i = 30 \cdot \left(\frac{(B-H)_{peak}}{R_{peak}}\right)_i \cdot k_i. \qquad (3)$$

The proportionality factor $k_{\mathrm{i}} = M(0)_{\mathrm{peak}}/(B\text{-}H)_{\mathrm{peak}}$ was calculated following the same numerical approach described in Sec. II. The volume under each peak was assumed cylindrical with radius R_{peak}, and thickness equal to the sample. For instance, from the peaks shown in Fig. 2(b) we found critical-current densities in the range of $J_c^{\mathrm{ab,i}}(0) \approx 1-2 \times 10^4$ A/cm^2 (with $k_{\mathrm{i}} \approx 0.17$), i.e., typical values reported for bulk melt-textured $YBa_2Cu_3O_7$ single-domain samples when H is parallel to the c axis.[19,20] The agreement between the critical-current densities obtained from different peaks is fairly good, taking into account the uncertainty in the determination of the extension of the local current loop $R_{\mathrm{peak,i}}$, and geometrical factors determining k_{i}.

An alternative way to determine J_c^{ab} and the effective J_c^{eff} is to compute the current distribution that produces the measured B_z profile by solving back the Biot-Savart law

$$B_z(r) = \frac{\mu_0}{4\pi} \int\int\int \frac{\mathbf{J}(r') \otimes (\mathbf{r} - \mathbf{r}')}{(r-r')^3} d^3r. \qquad (4)$$

For this purpose we used a general software tool ("CARAGOL"[21,22]), which has been widely tested for the determination of critical-current distributions in many geometries.[23] The calculation is also based on the critical state assumption, i.e., the maximum current density allowed is the critical current density J_c; however, the integral expression of Ampère's law rather than its differential form is used. The integral in Eq. (4) spans the whole scanned area, so no geometrical boundary conditions on the external shape of the sample need to be set. The problem is solved in the pseudo-3D approach, i.e., the currents are assumed to be planar and uniform along the z axis. Therefore, the current distribution computed is only the *ab* projection of the real current distribution in the foam. This implies that one could find a certain "equivalent" sample containing columnar holes and circulating planar currents that would give the same B_z profile. Hence, for certain purposes (e.g., the study of the influence of the pore size and disorder on the effective J_c^{eff};see below), we will be able to model the foams by their equivalent columnar hole systems. Figure 4 shows the current-density distribution computed for foam A in the remanent state. The critical-current density obtained from the observed local loops was $J_c^{\mathrm{ab,i}} \approx 1 \times 10^4$ A/cm^2, in good agreement with the value obtained from the magnetization slopes. The effective J_c^{eff} was estimated from the computed current-density distribution maps by evaluating the average current density along a line crossing the whole cross section of the sample, since the current distributions of the local loops cancel themselves and only the long-range current density prevails. The estimated value was $J_c^{\mathrm{eff}} \approx 0.5 \times 10^3$ A/cm^2, of the same order of magnitude as the J_c^{eff} determined from the slope of the background magnetization.

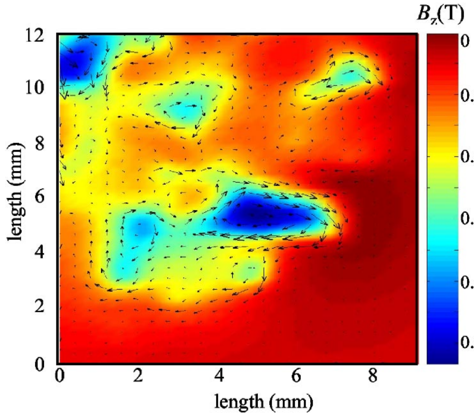

FIG. 4. Superposition of the remanent magnetization map $B_z(x,y)$ measured by Hall probe scanning and current distribution calculated through inversion of the Biot-Savart law ($\frac{1}{4}$ portion of foam A is shown).

In conclusion, the local critical-current density J_c^{ab} in the foam, which only depends on the vortex pinning and the nanostructure of the YBCO material, is typical of bulk melt-textured single-domain ceramics, while the effective current density J_c^{eff}, which describes the long-range currents extending over the sample, is typically one order of magnitude smaller than the physical local critical-current density.

To further understand the physical meaning of the effective current density J_c^{eff}, we have investigated how it is influenced by the sample porosity and pore disorder. Three foams (A, B, and C) having different $A_{\mathrm{S}}/A_{\mathrm{T}}$ were measured by Hall imaging, and the effective $J_c^{\mathrm{eff}}(0)$ in the remanent state determined using the critical state approach described above. Figure 5 shows the dependence of $J_c^{\mathrm{eff}}(0)$ with $A_{\mathrm{S}}/A_{\mathrm{T}}$. $J_c^{\mathrm{eff}}(0)$ has been normalized to the J_c^{eff} of a pore-free, bulk sample: $J_c^{\mathrm{eff}}(A_{\mathrm{S}}/A_{\mathrm{T}}=1) = J_c^{\mathrm{ab}}$(foam A) $\sim 2 \times 10^4$ A/cm^2. On the other hand, by solving the critical-state pattern of a theoretical infinitely long sample containing $n \times n$ (odd) cylindrical holes, distributed in a regular pattern (Fig. 5, inset), it can be shown that the $J_c^{\mathrm{eff}}(0)/J_c^{\mathrm{ab}}$ depends on $A_{\mathrm{S}}/A_{\mathrm{T}}$ as

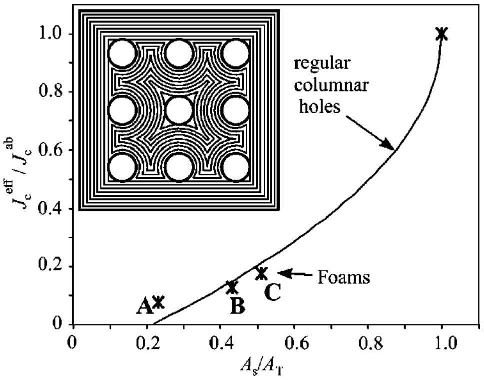

FIG. 5. (a) Effective current density $J_c^{per}(0)$ obtained from the remanent magnetic flux profiles as a function of the sample cross-section density A_S/A_T of different foams (*). Continuous line: Analytical J_c^{eff}/J_c^{ab} vs A_S/A_T dependence for a regular array of $n \times n$ cylindrical pores, Eq. (5), obtained by solving the flux distribution critical state pattern. Inset: e.g., critical state pattern in the remanence of an array of 3×3 cylindrical pores.

$$\frac{J_c^{eff}}{J_c^{ab}} = 1 - \frac{2}{\sqrt{\pi}}\left(1 - \frac{A_S}{A_T}\right)^{1/2}, \qquad (5)$$

independently of the number of holes, n. The factor $2/\sqrt{\pi}$ is the surface area density in the limit that holes touch each other and/or the area occupied by hole(s) A_h approaches the total sample area, $A_h \rightarrow A_T$. The decrease of the normalized effective current densities of foams with porosity is well described by the analytical expression (5), as can be observed in Fig. 5. This result suggests that the effective current is essentially determined by the amount of porosity of the foam, and little influenced by the pore disorder. To confirm this result, we studied further how the J_c^{eff}/J_c^{ab} (A_s/A_T) curve is affected by the pore distribution by simulating the critical state of samples with random distributions of holes, generated from an originally ordered pattern. The simulations, which will be presented elsewhere, showed that the degree of pore disorder in a foam has only a small influence on the J_c^{eff}/J_c^{ab} (A_s/A_T) dependence.

B. Field dependence of local and effective critical current densities

The field dependence of the local and effective critical current densities was investigated to further clarify the mechanisms underlying its behavior. The integrated magnetization field dependence $[\overline{B}\text{-}H](H)$ was determined from the Hall magnetization maps measured along a hysteresis loop. For example, Fig. 6(a) shows the $[\overline{B}\text{-}H](H)$ curves found for foam A after following two different cycles. The shape of these hysteresis loops is typical of melt-textured ceramics with a field-dependent critical-current density. The $[\overline{B}\text{-}H](H)$ obtained is a weighted average of the background (associated with J_c^{eff}) and local (associated with J_c^{i}) magnetizations, but we will show next that $[\overline{B}\text{-}H](H)$ describes mainly the background magnetization evolution. The absolute values of $(B\text{-}H)_{back,i}$ and local $(B\text{-}H)_{peak,i}$ under each i peak (Fig. 2) can be obtained from the Hall magnetic flux profiles measured at different magnetic fields to obtain the corresponding cycles. Figure 6(b) shows the $(B\text{-}H)_{peak,i}(H)$ cycles obtained from two different peaks observed in foam A [Fig. 2(b)], while Fig. 6(c) displays $(B\text{-}H)_{back,i}(H)/R_{b,i}$, where $R_{b,i}$ is the distance of the peak from the sample edge. The scaling of these ratios indicates that the background magnetic flux profiles follows indeed the critical-state model. Note that for all peaks $(B\text{-}H)_{peak,i} \gg (B\text{-}H)_{back,i}$. However, since the local peaks extend over much smaller areas than the background peak, the magnetic moment produced by short-

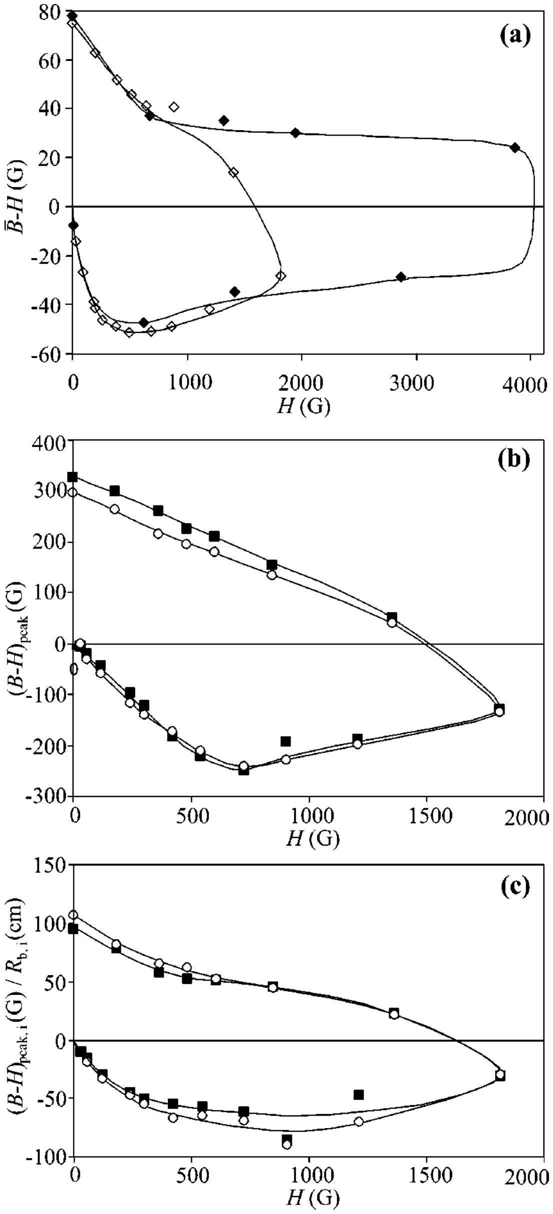

FIG. 6. (a) Two different integrated $(B\text{-}H)$ vs applied magnetic field cycles (foam A) obtained by Hall magnetic imaging system. (b) Magnetic field dependence of the local magnetization $(B\text{-}H)_{peak,i}(H)$ and (c) background magnetization normalized by the position of the peak with respect to the edge of the sample $(B\text{-}H)_{back,i}(H)/R_{b,i}$ [obtained from peaks (1) and (3) of foam A Hall profile].

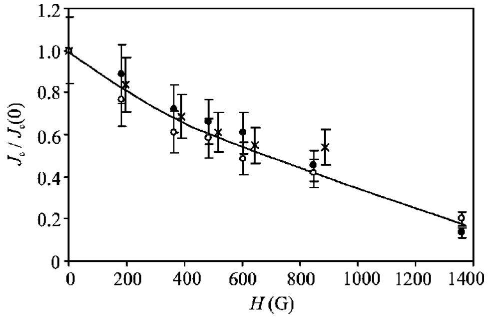

FIG. 7. Magnetic field dependence of the normalized effective critical current density $J_c^{\text{eff}}(H)/J_c^{\text{eff}}(0)$ (×) of foam A, estimated from the integral $[\overline{B\text{-}H}](H)$ cycle shown in Fig. 6(a). $J_c^{\text{eff}}(H)/J_c^{\text{eff}}(0)$ (○) calculated from the $(B\text{-}H)_{\text{back},3}(H)$ local background magnetization cycle shown in Fig. 6(b). Magnetic field dependence of the normalized local critical current density $J_c^{\text{i}}(H)/J_c^{\text{i}}(0)$, (●) obtained from the $(B\text{-}H)_{\text{peak},3}(H)$ cycle of Fig. 6(b). The particular $J_c^{\text{eff},3}$ and J_c^{3} values obtained from the magnetization peak 3 are representative of all other magnetization peaks.

range currents, $m_{\text{peak}} \propto (B\text{-}H)_{\text{peak}} R_{\text{loc}}$, is much smaller than the magnetic moment associated with the large-range ones. We have actually estimated that $m_{\text{peak}} \leqslant 10^{-2}\, m_{\text{back}}$. Therefore, the integrated magnetization can be associated with J_c^{eff} with a fairly good approximation.

The magnetic field dependence of the local and effective critical-current densities were, respectively, obtained from the $(B\text{-}H)_{\text{back,i}}(H)$ and $(B\text{-}H)_{\text{peak,i}}(H)$ hysteresis loops as $J_c^{\text{eff,i}}(H) \approx 30\Delta(B\text{-}H)_{\text{back,i}}(H).k/2R$ and $J_c^{\text{ab,i}}(H) \approx 30\Delta(B\text{-}H)_{\text{peak,i}}(H).k_{\text{i}}/2R_{\text{i}}$, where the constants k, k_{i} are defined through Eq. (1) and calculated with the methodology already described in Sec. III A. Figure 7 shows the normalized magnetic field dependencies of the local and effective critical-current densities found for foam A. For the sake of clarity, we present only the dependencies obtained from one of the peaks, but similar dependencies were obtained for the others. $J_c^{\text{eff}}(H)$ can be directly obtained also from the integrated magnetization cycle, since it represents basically the averaged background magnetization, as explained above. The $J_c^{\text{eff,i}}(H)$ values obtained from the individual peaks coincide indeed with the averaged $J_c^{\text{eff}}(H)$ dependence (Fig. 7).

Note also that the field dependencies of the local and effective critical current densities practically concur (Fig. 7). This coincidence might be expected, since there is only one physical critical-current density in the material, whose field dependence is governed by flux pinning in the $\text{YBa}_2\text{Cu}_3\text{O}_7$ material.[24] The effective critical-current density is reduced as compared to J_c^{ab} only due to the porosity of the foam. This situation is different from that of multigranular superconducting ceramics,[9,25] which present a "real" double critical state resulting from a long-range (percolative) intergranular current density and a local, intragranular current density. In that case the magnetic field dependence of the two critical-current densities is very different, since $J_c^{\text{intra}}(H)$ is ruled by vortex pinning, while $J_c^{\text{inter}}(H)$ is determined by the grain boundary behavior.

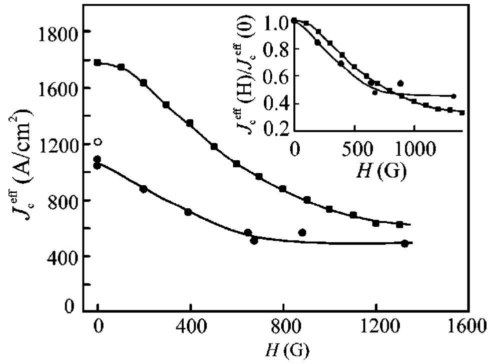

FIG. 8. Magnetic field dependence of the effective critical-current density $J_c^{\text{eff}}(H)$ of foam A (●), determined from the $[\overline{B\text{-}H}](H)$ Hall cycle, and foam C (■), obtained from the magnetometer $m(H)$ hysteresis loop. (○) $J_c^{\text{per}}(0)$ of foam A calculated from the slope of the remanent magnetization Hall profile. Inset: normalized $J_c^{\text{eff}}(H)/J_c^{\text{eff}}(0)$ for the same foams.

Finally, we investigated the field dependence of $J_c^{\text{eff}}(H)$ of two foams (A and C), with different porosities $A_{\text{S}}/A_{\text{T}}$ (Fig. 8). The $J_c^{\text{eff}}(H)$ of foam A, containing large size pores ($\approx$2.6 mm), could only be determined from the $[\overline{B\text{-}H}](H)$ Hall probe measurements, due to size restrictions of the magnetometer sample holder. Note that the $J_c^{\text{eff}}(0)$ value obtained from the magnetization cycle is similar to the $J_c^{\text{eff}}(0)$ determined from the slope of the remanent magnetization Hall profile (Sec. III A), hence validating the two calculation methods. The $J_c^{\text{eff}}(H)$ dependence of foam C, which contained much smaller pores, could be obtained from the direct measurement of the magnetic moment cycle $m(H)$ with the magnetometer, as $J_c^{\text{eff}}(H) = 30\Delta m(H)/2RV$, V being the total sample volume. Notice that though $m(H)$ integrates all contributions, since $m_{\text{peak}} \ll m_{\text{back}}$ as we argued before, the critical-current density obtained from the Δm cycle is approximately equal to $J_c^{\text{eff}}(H)$. The normalized magnetic field dependence $J_c^{\text{eff}}(H)/J_c^{\text{eff}}(0)$ for both foams is similar (see the inset to Fig. 8). This result confirms that the pinning mechanisms determining the field dependence of long-range currents in all foams are similar, and no major modifications of the bulk flux pinning behavior occurs associated with the modified pore sizes.

IV. CONCLUSIONS

The critical state appearing in single-crystalline superconducting $\text{YBa}_2\text{Cu}_3\text{O}_7$ foams can be described by an effective critical-current density producing a background magnetization, and the physically local critical-current density giving rise to a superposed local magnetization peaks. We were able to evaluate both critical-current densities applying the critical-state model, either from the Hall magnetization profiles, or by using the Biot-Savart inversion method, assuming in both cases in-plane currents. The effective critical-current densities are typically reduced by a factor of 5–10 as compared to the local critical-current densities in the foams investigated. We have shown that the planar component of the long-range current depends on the surface porosity in a similar way to the law found for an effective current in a sample containing $n \times n$ ordered hollow cylinders. Hence, the amount of porosity, rather than pore disorder, is the main parameter controlling the effective critical-current density. The dependence of the effective and local critical-current densities with the magnetic field is very similar, and independent of the porosity. This indicates that though two critical-current densities have been used to describe the irreversible behavior of foams, vortex pinning, depending on the $YBa_2Cu_3O_7$ microstructure, is the only microscopic physical mechanism ruling their magnetic behavior.

ACKNOWLEDGMENTS

This work was supported by the Generalitat de Catalunya (Catalan Pla de Recerca 00206 and CeRMAE) and by the MCYT (MAT2002-02642). One of us (E.B.) thanks the CSIC (Consejo Superior de Investigaciones Científicas), Spain, for the financial support of the I3P Contract Program.

---

[1] C.P. Bean, Phys. Rev. Lett. **8**, 250 (1962).

[2] E. H. Brandt, in *Physics and Materials Science of Vortex States, Flux Pinning and Dynamics*, edited by R. Kossowsky *et al.* (Kluwer Academic, Dordrecht, 1999), p. 81.

[3] E.H. Brandt, M. Indenbom, and A. Forkl, Europhys. Lett. **22**, 735 (1993).

[4] J.R. Clem and A. Sánchez, Phys. Rev. B **50**, 9355 (1994).

[5] E.S. Reddy and G.J. Schmitz, Supercond. Sci. Technol. **15**, L21 (2002).

[6] E.S. Reddy, M. Herweg, and G.J. Schmitz, Supercond. Sci. Technol. **16**, 608 (2003).

[7] T. Verhaege *et al.*, in *Handbook of Applied Superconductivity*, edited by B. Seeber (Institute of Physics, Bristol, 1998), pp. 1691–1702.

[8] P. Tixador, X. Obradors, R. Tourniers, T. Puig, D. Bouraults, X. Granados, J.M. Duval, E. Mendoza, X. Chaud, E. Varesi, E. Beaugnon, and D. Isfort, Supercond. Sci. Technol. **13**, 493 (2000).

[9] J. Clem, Physica C **153–155**, 50 (1988).

[10] H. Fang, Y.X. Zhou, K. Ravi-Chandar, and K. Salama, Supercond. Sci. Technol. **17**, 269 (2004).

[11] S. Jin, T.H. Tiefel, R.C. Sherwood, M.E. Davis, R.B. van Dover, G.W. Kammlott, R.A. Fastnacht, and H.D. Keith, Appl. Phys. Lett. **52**, 2074 (1988).

[12] K. Salama, V. Selvamanickan, and D.F. Lee, in *Processing and Properties of High-Tc Superconductors*, edited by S. Jin (World Scientific, Singapore, 1993), Vol. 1, Chap. 5, pp. 155–211.

[13] X. Obradors, R. Yu, F. Sandiumenge, B. Martínez, N. Vilalta, V. Gomis, T. Puig, and S. Piñol, Supercond. Sci. Technol. **10**, 884 (1997).

[14] E.S. Reddy and T. Rajasekharan, Supercond. Sci. Technol. **11**, 523 (1998).

[15] X. Granados, S. Sena, E. Bartolomé, A. Palau, T. Puig, X. Obradors, M. Carrera, J. Amorós, and H. Claus, IEEE Trans. Appl. Supercond. **13**, 3667 (2003).

[16] A. Sánchez and C. Navau, Phys. Rev. B **64**, 214506 (2001).

[17] E.M. Gyorgy, R.B. van Dover, K.A. Jackson, L.F. Schneemeyer, and J.V. Waszcak, Appl. Phys. Lett. **55**, 283 (1989).

[18] H.P. Wiesinger, F.M. Sauerzopf, and H.W. Weber, Physica C **203**, 121 (1992).

[19] X. Obradors, R. Yu, F. Sandiumenge, B. Martínez, N. Vilalta, V. Gomis, T. Puig, and S. Piñol, Supercond. Sci. Technol. **10**, 884 (1997).

[20] J. Wang, I. Monot, X. Chaud, A. Erraud, S. Marinel, J. Provost, and G. Desgardin, Physica C **304**, 191 (1998).

[21] M. Carrera, J. Amoros, A.E. Carrillo, X. Obradors, and J. Fontcuberta, Physica C **838**, 539 (2003).

[22] On line at: www.jaumetor.upc.es/Caragol

[23] M. Carrera, J. Amorós, X. Obradors, and J. Fontcuberta, Supercond. Sci. Technol. **16**, 1187 (2003).

[24] B. Martínez, T. Puig, A. Gou, V. Gomis, S. Piñol, J. Fontcuberta, X. Obradors, and G. Chouteau, Phys. Rev. B **58**, 15 198 (1998).

[25] M. Tinkham and C.J. Lobb, Solid State Phys. **42**, 91 (1989).